Section 1
THE OMEGA UPGRADE

Part II: Preliminary Design and Target System

In the first article of this issue we present a description of the preliminary design of the OMEGA Upgrade, which is now near completion. This design has evolved significantly over the past two years as a result of numerous reviews, efforts to control costs, the elimination of unnecessary complexity, and the development of smoothing by spectral dispersion (SSD). For example, the multisegmented amplifiers described in the last issue of the LLE Review have been replaced with disk amplifiers of conventional design, and the location of the frequency-conversion crystals has been changed from the target-mirror structure to the laser bay.

We have now converged upon a basic concept that will provide the laser energy, uniformity, and pulse shape needed to enable LLE to carry out an important series of ignition-scaling experiments in the 1990s. We have also identified portions of the preliminary design where further theoretical and experimental investigations and prototyping are necessary before arriving at the final design.

In the second article we describe the target system of the OMEGA Upgrade, including the experimental target chamber, the target-positioning and viewing systems, the vacuum system, and the target diagnostic systems. In addition, we report the results of a study carried out with Grumman Aerospace of possible radiological effects on the target chamber and the surrounding area.

1.A OMEGA Upgrade Preliminary Design

In this article we give a general description of the baseline design for the OMEGA Upgrade, including its motivation, capabilities, and limitations. We start by showing how the theoretical desire for a shaped pulse, coupled with the practical limitations inherent in the third-harmonic-generation process, leads to a co-propagated main-pulse/foot-pulse system, and how the parameters of the desired UV pulse on target lead to requirements imposed on the IR portion of the system. These considerations also lead to the anticipated performance parameters of the system. We then proceed to give a brief description of each of the main subsystems, working from the oscillators to the target chamber. We include a discussion of some physical processes, such as laser-beam propagation, stimulated rotational Raman scattering, and transverse stimulated Brillouin scattering, and show that these processes do not adversely affect the viability of the upgrade design.

Number of Beams and Pulse Shaping

A key parameter is the number of beams on target. For direct drive, this number is by no means arbitrary if a reasonably symmetric structure in the target area is desired. Given any number of beams (N), we can use a computer code (REPEL) to find a reasonable placement configuration by treating the beams as identical point charges on a sphere and minimizing their potential energy; however, with the exception of a small set of values of N, this does not yield solutions with adequate symmetry. The most practical configurations are based on subdivisions of the Platonic solids: e.g., placing four beams on each face of the cube gives the current OMEGA configuration; placing one beam on each vertex and face of a dodecahedron (or equivalently an icosahedron) gives a 32-beam configuration (known as a truncated icosahedron), which maps on to the 32 faces of a soccer ball; and placing one beam at each vertex of a soccer ball (5 for each of the 12 pentagonal faces) yields a symmetrical 60-beam configuration where all beams are equivalent; combining the 32 faces and 60 vertices of the soccer ball gives a 92-beam configuration, and so on. We have adopted the 60-beam configuration as it provides significant additional uniformity over the existing 24-beam system for minimum additional complexity. [We do not claim originality: the tobacco necrosis virus, for example, is a simple shell of 60 identical protein molecules,[1] and the same structure has been proposed for a molecule containing 60 carbon atoms ("buckminsterfullerene").[2]] It is also important to note that the beam aperture required to supply 30 kJ in 60 beamlines is sufficiently small that segmentation can be avoided, and use can be made of optical components having a reasonably low cost-per-unit area.

The detailed 60-beam irradiation geometry selected is shown in Fig. 39.1, and referred to as a "stretched-soccer-ball" configuration. This is arrived at by first placing five beams at the corners of each of the 12 pentagonal faces of a soccer ball, and then adjusting the one free parameter in this geometry, namely the distance of a beam from the center of a pentagon. This distance is increased slightly from that corresponding to the ideal soccer-ball geometry, such that the distance between neighboring beams measured around a pentagonal face (*A* in Fig. 39.1) is a factor of 1.2 greater than the distance *B* on a hexagonal face. The hexagonal faces are no longer truly hexagonal, but irradiation uniformity is improved because clustering around the pentagonal faces is eliminated. This geometry provides enough uniformity to meet the theoretical on-target uniformity requirement of 1%–2% rms, but there are not so many beams that the system is too complex to be viable.

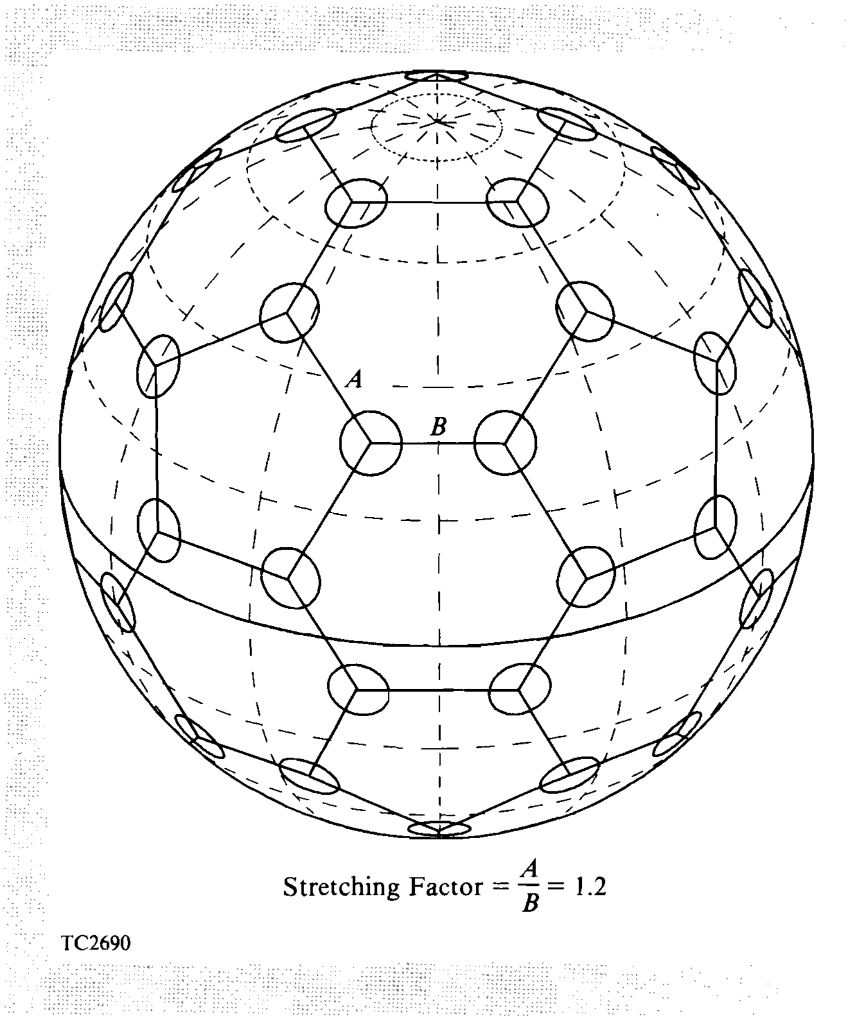

Fig. 39.1
60-beam stretched-soccer-ball geometry proposed for the OMEGA Upgrade.

Generation of the shaped pulse required for an efficient ablative target implosion presents a significant problem because of the limited dynamic range of all known practical frequency-tripling schemes: quadrature schemes[3] permit high-dynamic-range frequency doubling but not tripling, while the polarization-bypass tripling scheme,[4] which has an unlimited dynamic range, is too sensitive to misalignment to be practical for use with KDP. It is useful to approximate the ideal shaped pulse [shown dashed in Fig. 39.2(a)] as the sum of two Gaussians, a "foot" pulse followed by a "main" pulse: in practice, pulse-shaping techniques can be applied to these Gaussians to provide a closer approximation to the dashed curve, especially around the time that the two pulses merge. The peak powers of the foot and main pulses are typically in a ratio of 1:20. One option is to select the frequency-conversion crystals to provide efficient tripling of the main pulse, and compensate for low tripling efficiency in the foot pulse by generating extra infrared energy in the foot; however, this is wasteful of laser energy. Another option is to build separate laser systems for the two pulses, from the oscillator to the focusing lenses, but this would entail considerable extra complexity and additional cost, especially around the target chamber.

Co-propagation

The solution that has been incorporated into the upgrade design is a co-propagated laser,[5] in which a small-diameter foot pulse of cylindrical cross section propagates inside an annular main pulse [see

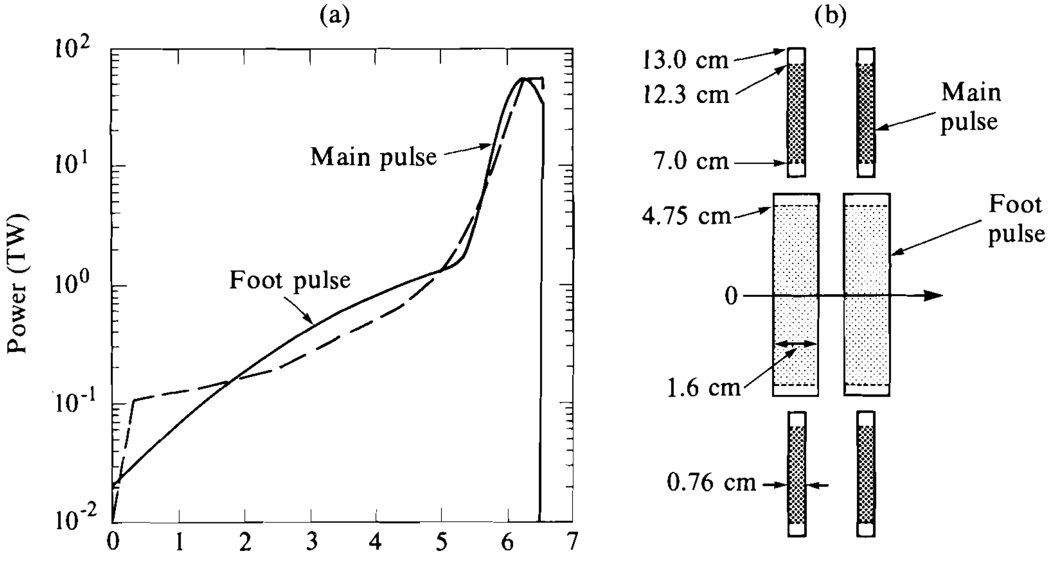

TC2616

Fig. 39.2
Dual-pulse basis of upgrade design. (a) Double-Gaussian temporal profile of laser power formed by superposing a long foot pulse and a short main pulse, approximating the ideal shaped pulse shown dashed; (b) cross section of co-propagated foot and main beams at the frequency-conversion crystals.

Fig. 39.2(b)]. Each beam is azimuthally symmetric about the propagation direction (shown as an arrow in the figure). Co-propagation begins at the front end of the laser, where two oscillator pulses are first amplified in separate driver lines, and then appropriately apodized and combined into a single beam, which is maintained through the remainder of the laser system. At the end of the infrared portion of the system, conversion crystals of two different thicknesses are mounted one inside the other, each crystal optimized for the beam incident upon it. The beam dimensions at the crystals are chosen so that the UV energy loading, multiplied by a safety factor to accommodate UV hot spots, does not exceed the damage threshold of the high-reflectance and anti-reflection coatings following the crystals.

The shaded areas in Fig. 39.2(b) represent nominal beam areas and the solid edges indicate the clear aperture. Beam energy will actually spread a little outside the shaded areas, but the main and foot beams will remain distinct. The IR beam emerging from the last amplifier is expanded to accommodate the lower UV damage thresholds. Figure 39.2(b) is schematic; the method by which the crystals are mounted is not discussed here. The use of two separate crystals has been found to be more cost effective than the single "top-hat" crystals proposed in Ref. 5.

One other advantage of propagating the foot pulse through just a portion of the whole aperture is that while the total power ratio is ~20:1, the intensity ratio on the crystals is only 5:1, allowing for thinner foot-pulse crystals than would otherwise have been called for. It is important to note that this co-propagation configuration only works because we are using distributed phase plates (DPP's)[6,7] at the focusing lenses; since each DPP element irradiates the whole target, the locations of the foot and main beams in the near field are immaterial. Without DPP's, the target would be irradiated with annular main beams, which would be unacceptable from the point of view of uniformity. DPP's are also essential components for SSD, a technique for obtaining good irradiation uniformity on target that has been developed at LLE[8] and forms an integral part of the upgrade design.

Performance Parameters

Parameters anticipated for the main and foot pulses are listed in Table 39.I, for a main-pulse width ranging from 0.5 to 0.75 ns and a foot-pulse width from 3 to 5 ns. They are derived by working back from the energy and pulse shape needed at the target. The design of the upgrade is based on a requirement that 24 kJ of UV main-pulse energy be available on target in the front 80% of a Gaussian whose full width can vary in the range 0.5 ns–0.75 ns, with 6 kJ of foot-pulse energy in the front half of a Gaussian of full width 5 ns. Using a measured DPP efficiency of 79% (into the central disk of the focal spot) and assuming a 9% transport loss (including a 4% diagnostic pickoff and 0.5% from each coated surface), one can calculate the UV energy required from each crystal. Knowing the (intensity-dependent) pulse shortening produced in the crystals, one can then work back to find the IR energies and pulse widths required at the crystal input. Numerical modeling of all portions of the system is used to calculate

Table 39.I Anticipated performance of OMEGA Upgrade

	Main Pulse		Foot Pulse	
Beam area (cm^2)	321		71	
Temporal shape	Gaussian		Half-Gaussian	
Crystal thickness L (cm)	0.76		1.6	
UV FWHM (ns)	0.50	0.75	3.0	5.0
IR FWHM (ns)	0.56	0.9	3.3	5.56
Nominal IR intensity on crystal I_0 (GW/cm^2)	5.47	3.38	0.98	0.98
Normalized IR intensity of most intense ray(a)	5.14	3.18	4.08	4.08
Operating point of most intense ray(b)	M_1	M_2	F	F
Frequency conversion efficiency (%)	80	70	75	75
IR energy per beam on to crystals (J)	977	977	116	194
UV energy per beam out of crystals (J)	782	684	87	146
UV energy per beam on target (J)(c)	564	493	62.7	105
Average UV energy loading after crystals (J/cm^2)	2.4	2.1	1.2	2.1
AR damage fluence for full Gaussian (J/cm^2)	3.8			6.8
Peak UV power on target (TW)	63.5	37.1	2.4	2.4
Total UV energy on target (kJ)	33.8	29.6	3.8	6.3
Truncated UV energy on target (kJ)(d)	27.1	23.7	3.8	6.3

(a) 0.9394 $I_0(L/0.76)^2$. See Fig. 39.3

(b) See Fig. 39.3

(c) Assumes a 9% transport loss and a DPP efficiency of 79% (into the central disk of the focal spot)

(d) With truncation of the last 20% of the main-pulse UV energy

TC2631

the pulse shapes and other parameters at the oscillators required to give the desired pulse shape on target.

The foot pulse is truncated at its peak to reduce the energy loading on coatings, as the second half of the foot-pulse Gaussian is obviously irrelevant to the target implosion; however, since the damage fluences associated with truncated laser pulses have not yet been measured, the system is designed conservatively so that it will not damage at the fluences that would result if the electro-optic device that truncates the pulse were to fail. The weakest anti-reflection coating in the UV subsystem is the sol-gel coating on the final KDP surface; its damage threshold for full Gaussian (i.e., untruncated) pulses varies from 3.8 to 6.8 J/cm^2 for pulse widths of 0.5 to 5 ns. The coating will handle the anticipated UV energy loadings at both pulse widths, even if the foot pulse is not truncated, with a safety factor of 1.6:1–1.8:1 to accommodate UV hot spots (i.e., modulations of the near-field UV intensity distribution that might arise from diffraction in the system). It is also planned to truncate the last 20% of the main-pulse Gaussian, which also is of little value to the implosion. Again, the system is designed conservatively so that it will handle a non-truncated Gaussian main pulse, although under routine operating conditions the last 20% of the UV energy will be truncated.

Table 39.I gives the parameters associated with a Gaussian main pulse; this is also convenient because the intensity, pulse width (FWHM), area, and energy are then related in the obvious way. The actual, truncated energies that will be obtained on target are given in the bottom line. The total energy available will depend on the combination of main- and foot-pulse widths selected; however, it is evident that, for the longer foot pulse, a total of 30 kJ of useful on-target energy will be available throughout the range of main-pulse widths.

The parameters given in Table 39.I allow for reasonable flexibility in pulse shaping. Greater flexibility is possible, since pulses as short as 100 ps and as long as 10 ns can be obtained from the main- and foot-pulse oscillators, respectively. However, with pulse widths outside the ranges indicated in the table, less than 30 kJ will be available. For shorter pulses the system is intensity limited, while for longer pulses it is energy limited in the IR and experiences a lower frequency-conversion efficiency. The system is potentially capable of producing an extra 3 kJ in the main pulse at the shorter pulse width of 0.5 ns (27 kJ rather than the 24 kJ required), because higher conversion efficiencies are obtained at higher input intensities, but this will only be possible if the UV coatings can handle the extra loading (2.4 rather than 2.1 J/cm^2).

The characteristics of the frequency-conversion crystals are shown in Fig. 39.3, for rays of a single intensity I. By using the intensity normalized to the thickness of the main-pulse crystals on the abscissa $I' = I(L/0.76\ \text{cm})^2$ where L is the crystal thickness, the same curve can be applied to both the main pulse and the foot pulse to a good approximation. (The calculation is exact for $L = 0.76$ cm; about 3% lower efficiencies are actually obtained for the foot pulse due to greater IR absorption in the thicker crystals.) The operating points corresponding to the intensities found at the peaks of the pulses are indicated for the 0.5-ns and 0.75-ns main-pulse options (M_1 and M_2, respectively), and for the foot pulse (F, independent of pulse width). Larger overall efficiencies than 82.5% could be obtained for the integral over a Gaussian temporal shape for the 0.5-ns main pulse by operating to the right of M_1, but we prefer to avoid this regime because of an increased sensitivity to depolarization in the beam. The point M_2 for the longer 0.75-ns main pulse lies to the left because we are assuming an unchanged infrared energy out of the amplifiers; M_1 is approximately the current operating point on OMEGA. The foot pulse would also operate at M_1 with a choice of 1.8-cm-thick crystals; however, we plan to save costs by using existing 1.6-cm-thick OMEGA crystals, each of which can be cut in half and reworked, and operating instead at point F with $\approx 5\%$ lower conversion efficiency. (The figure of 74.7% quoted for the integration over a Gaussian takes IR absorption fully into account.) It is also worth noting that it is undesirable to design the crystals with the operating point of the

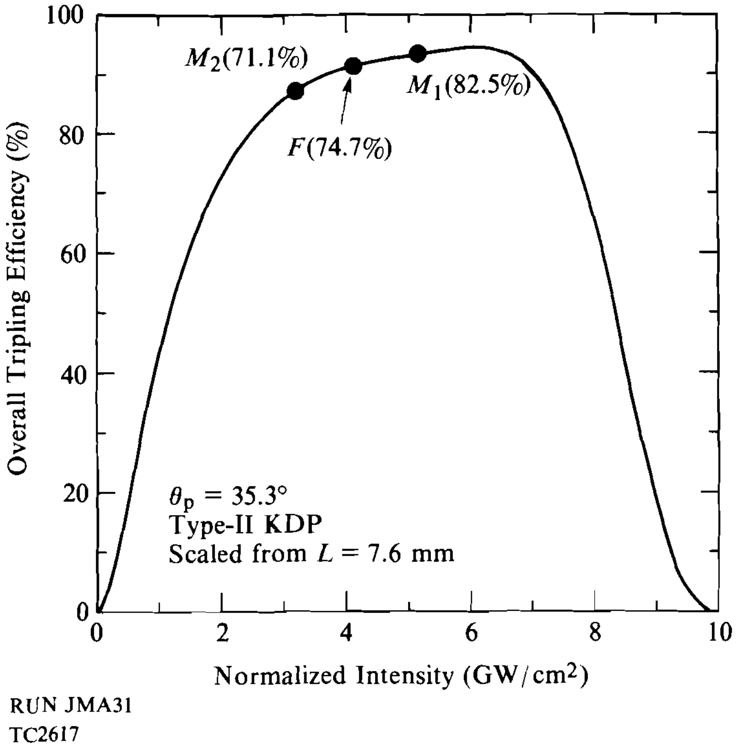

Fig. 39.3
Ideal third-harmonic generation efficiency for a single ray as a function of normalized intensity I' [$= I(L/0.76)^2$ where L is the crystal thickness in centimeters]. M_1, M_2, and F indicate operating points for the main pulse (0.5 and 0.75 ns) and for the foot pulse. Corresponding averages over a temporal Gaussian (or equivalently a half-Gaussian) are shown in parentheses.

system at maximum energy too far to the left in Fig. 39.3, because the falloff of conversion efficiency at high intensity serves to protect the system against the formation of near-field UV hot spots from near-field IR hot spots.

Overall Layout of Upgrade

The overall layout planned for the upgrade is illustrated in Figs. 39.4 and 39.5. The need to fit all the hardware (including the extra amplifiers, the extra beamlines, and a larger target chamber) into existing building space has led to a substantial rearrangement. The oscillators and driver lines, including SSD hardware and the means to combine the two beams into a single co-propagated beam, will be located in the capacitor bays beneath the floor of the existing laser bay. The co-propagated beam will be transported to the laser bay and split into 15 beams in two stages, a three-way split followed by a five-way split, with an existing OMEGA 64-mm rod amplifier following each split (amplifier stages A and B of Fig. 39.5). All beam splitters will have motorized, automated polarization control to provide for accurate energy balance. The 15 beams will be propagated through existing 90-mm OMEGA amplifiers (stage C) and spatial filters in the center of the bay in three stacks of five each. Each beam is split four ways at the end of the bay, at which point the 60 resulting beams pass through assemblies that permit ±1.5 m of gross path-length adjustment needed to compensate for the inequality in transport paths to the target chamber and to provide precision beam-timing capability.

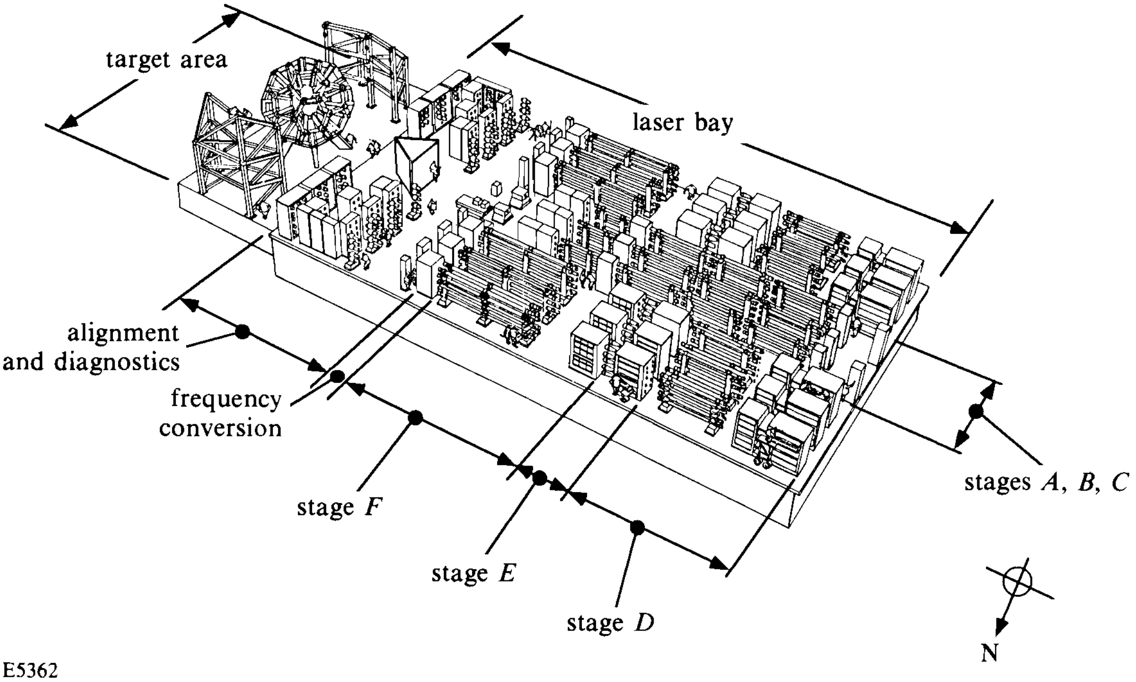

Fig. 39.4
Perspective view of the OMEGA Upgrade.

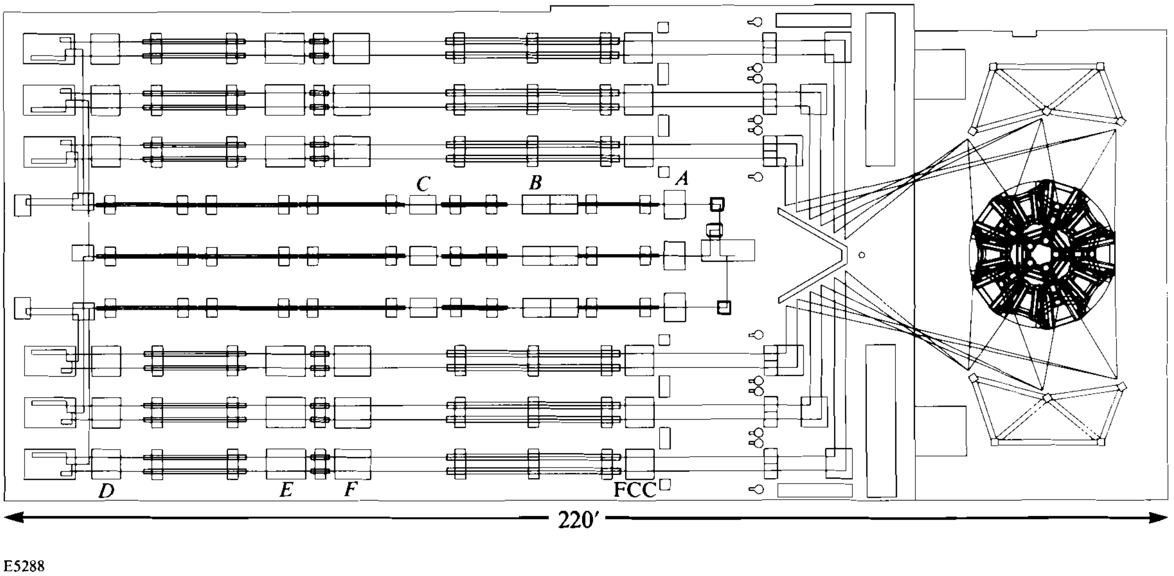

Fig. 39.5
Layout of the OMEGA Upgrade. The location of four stages of rod amplifiers (*A*-*D*), two stages of disk amplifiers (*E*,*F*) and the frequency-conversion crystals (FCC's) are indicated.

The 60 beams then propagate back near the outside of the bay in six clusters of ten beams (two wide, five high); each beam will pass through another 90-mm rod amplifier (stage *D*), through two stages of disk amplifiers (*E* and *F*), and onto the frequency-conversion crystals (FCC's). Thin-film polarizers will be used immediately prior to the crystals to ensure that the correct linear polarization is incident upon the crystals. After frequency conversion, a small fraction of the energy of each beam will be split off for energy diagnostics at the fundamental, second harmonic, and third harmonic, with separate measurements for the foot and main pulses; the UV beams will then be transported to the target chamber, half approaching from each side rather than all directly from the V-shaped structure as presently configured.

At each stage, spatial filtering will be used to remove high-spatial-frequency noise from the beam and to ensure correct image relaying.[9] Image relaying is also important for SSD, to prevent different frequencies from wandering excessively across the beam cross section due to the grating-induced differences in their propagation directions, and to prevent the formation of intensity modulations through interference effects. In particular, the annular dead zone at the co-propagation apodized aperture (between the main and foot beams) must be imaged to the dead zone between the crystals. The size of the dead space or "anti-mix" zone between the foot and main pulses is chosen to be sufficient to prevent spatial overlap of the two pulses, but is otherwise minimized to save on the aperture of disks and other optical components.

The IR portion of the system is analyzed in detail using two codes: RAINBOW, a ray-tracing code, which includes experimentally measured amplifier gain profiles and gain saturation,[10,11] and MALAPROP,[12-14] which models diffraction and nonlinear effects (including amplitude and phase noise) in various optics and spatial filters. Given the beam parameters required at the input to the frequency-conversion crystals, we can iteratively calculate the IR parameters required at the input to the driver line.

Oscillators and Driver Lines

The foot pulse will be generated in a self-seeded, single-mode, Nd:YLF Q-switched oscillator. The monomode character of the emission of this oscillator is guaranteed through intracavity etalons and an extended low-level prelase phase. The oscillator will emit 10- to 20-ns pulses from which 3- to 6-ns shaped pulses will be carved out. For the main pulse the output of a cw mode-locked master oscillator will be used to seed a regenerative amplifier. Flexibility of adjustment of the pulse width from 500 to 900 ps will be provided by the insertion of intracavity etalons into the cw master oscillator. The central wavelengths of the two oscillators will be stable to 0.1 Å, which will ensure less than 1% degradation of the third-harmonic conversion efficiency.

The synchronization of the main and foot pulses will be achieved through a combination of (a) synchronized Q-switches for the main-pulse and foot-pulse generators; (b) two rf-synchronized, cw mode-locked, master oscillators seeding two regenerative amplifiers for the main pulse and an auxiliary short-pulse switching laser; (c) a pulse generator with a ps-precision delay; and (d) optoelectronically triggered high-voltage pulse generators. These latter pulse generators drive Pockels cells that are used to shape the foot pulse as well as to truncate the foot and main pulses.[15,16]

There are presently two designs under consideration for the main-pulse and foot-pulse driver lines: one is based on the present OMEGA driver line with only minor modifications; the other is based on a large-aperture, imaging, unstable resonator operating as a regenerative amplifier. Both designs incorporate SSD gratings and an rf phase modulator.[8] The trade-off between the two driver-line designs will be based on the results of experiments on large-aperture regenerative amplifiers, which have recently been initiated. Apodization of the driver lines prior to combination into a single co-propagated beam will be performed using LLE-developed liquid-crystal apodizers.[17,18]

Disk Amplifiers

The disk amplifiers will be of conventional box geometry.[19,20] A 15-cm-diameter stage will be followed by a 20-cm-diameter stage, each containing four disks (see Fig. 39.6). The clear aperture of the final amplifier is set by damage constraints, specifically the sol-gel anti-reflection coating on the input lens to the final spatial filter that damages when the main pulse reaches 9.8 J/cm^2 (of untruncated energy). The 15-cm stage provides a main-pulse saturated gain of 3.1, and the 20-cm stage a gain of 2.3. Saturated gains for the foot pulse will be slightly lower because the longer pulse operates at a higher fluence.

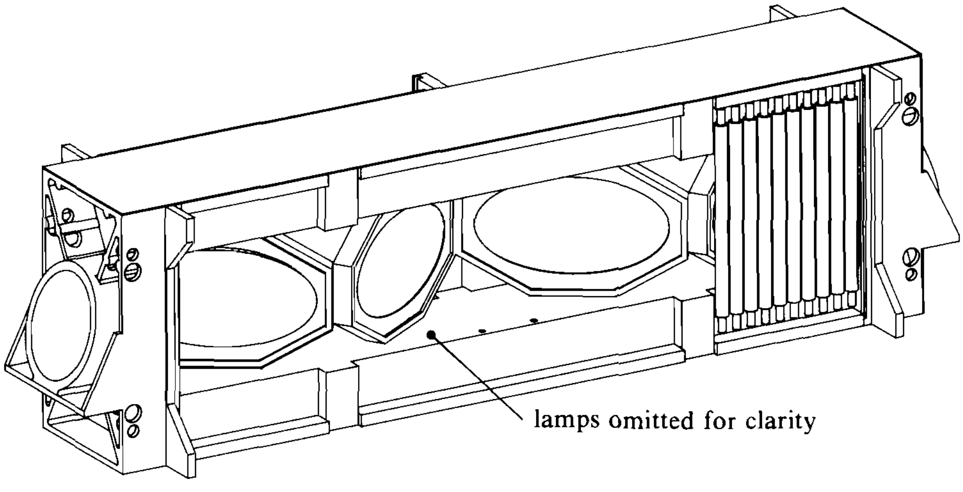

Fig. 39.6
Schematic of a 20-cm-aperture disk amplifier.

Both stages will be able to use the same power-conditioning pulse-forming network. The stages will be separated by a beam expander rather than a spatial filter, and therefore have to be considered as a single stage in calculations of the B-integral. (The B-integral is the phase delay accumulated in a high-power laser beam due to the nonlinear, intensity-dependent refractive index; small values of B are desired in order to minimize the possibility of self-focusing.) The ΔB for the combined stage (pinhole to pinhole) is a modest 1.6 for the main pulse, less than the traditional limit per stage of 2.0.[21] The B-integral is not a consideration for the foot pulse, which operates at a lower intensity than the main pulse. Cooling times for the amplifier disks will be sufficiently short to permit a 1-h shot cycle.

The disk-amplifier design makes use of water-cooled flash lamps in order to operate with a high storage efficiency, for reasons of economy. The modular nature of the design allows for the rapid change of gain medium and/or pump modules within the shot cycle.

In earlier designs for the upgrade we considered using 15 multisegmented amplifiers (MSA's), each amplifying four beams.[5] However, in order to obtain power balance on target,[22] it is necessary to balance the amplifier gain between individual beamlines. The MSA concept, while delivering improved efficiency, did not lend itself to adjustment of individual beamline gains. For this reason, and because of the higher gain offered by single-beam box amplifiers, we have opted for the box amplifier in our current design. We are completing construction of a prototype MSA, which we will test as part of our laser-development program in parallel with upgrade design activity.

Location of Frequency-Conversion Crystals

The frequency-conversion crystals will be placed in the laser bay, after the IR portion of the system but before transport to the target area. Earlier designs for the OMEGA Upgrade considered placement of the crystals on the target structure just after the last reflecting mirror, as on NOVA, except that the crystals would not be placed so close to the focusing lenses. This has the advantages of totally avoiding the need for high-reflectance UV coatings and minimizing the propagation distance of UV radiation, but these are outweighed by a number of drawbacks, some of which are listed here: (a) it is uncertain whether 0.76-cm-thick crystals of ~30-cm aperture can be mounted in all orientations without encountering problems associated with gravitationally induced stress; (b) the target-mirror structure would be crowded by a large number of components; (c) the IR beam could suffer some depolarization as a result of the multiple reflections off transport mirrors; (d) accurate measurement of the main-beam and foot-beam energies and conversion efficiencies would be precluded; (e) there would be a risk of crystals and associated optics being damaged by ghosts from the focusing lenses; and (f) the crystals would not be located near an image relay plane.

All of these drawbacks are avoided by placing the crystals in the laser bay, vertically mounted. The critical factor determining the total energy capability of the system now becomes the damage threshold of high-reflectance UV coatings. Coatings for which this threshold is 3.0 J/cm^2 at 0.5 ns, for an untruncated UV pulse, have been demonstrated at LLE.[23] With modest technological development it is anticipated that the design goal of 3.8 J/cm^2 will be achieved.

Beam Propagation

The baseline design for the mirror configuration required to transport the UV beams to the target chamber uses the system shown in Fig. 39.5, which is similar to that now used on OMEGA and has the advantages of simplicity and low cost. However, two concerns have been raised that could lead to amendment of this design should either prove to be warranted.

The first concern is the possibility of stimulated rotational Raman scattering (SRRS)[24] associated with the nitrogen in the ~40-m-long air path from the frequency-conversion crystals to the target chamber. For a nondepleted pump-laser beam with time-dependent intensity $I_L(t)$, the intensity I_S of the Stokes wave grows exponentially with propagation distance z as

$$I_S\,(z,\,t) \;=\; I_{So}\,\exp[g_R I_L(t) z], \tag{1}$$

where g_R is the steady-state gain coefficient for the SRRS process in air and I_{So} is the optical noise field at $z = 0$. Equation (1) is valid provided that the pulse width τ_L of the pump laser is long in comparison with the response time τ_R of the SRRS process. For short laser pulses ($\tau_L \lesssim 10\ \tau_R$) the scattering is transient, and Eq. (1) is replaced by the following equation[25]:

$$I_S(z,\,t) \;=\; I_{So}\,\exp\,[2(g_R\, I_L(t)\; zt/\tau_R)^{1/2} \;-\; t/\tau_R]. \tag{2}$$

Substantial amplification of the optical noise field must occur before significant scattered light is detectable. For typical conditions, the gain factor G [i.e., the argument of the exponential in Eqs. (1) and (2)] must reach approximately 30–35. We can estimate G by using parameters reported for air[24,26] and extrapolated to our conditions: g_R = 2.5 cm/TW at 1054 nm and 7.5 cm/TW at 351 nm, and τ_R = 0.133 ns. Clearly Eq. (1) applies for the foot pulse and Eq. (2) for the main pulse. To obtain worst-case estimates, we use the peak UV intensities I_{Lo} out of the frequency-conversion crystals, obtained from the peak IR intensities at the crystal input assuming a 90% instantaneous tripling efficiency (see Fig. 39.3), and we neglect transport losses due to diagnostic pickoffs. From Table 39.I we find that I_{Lo} = 4.63 GW/cm^2 for the 0.5-ns main pulse, and 0.83 GW/cm^2 for the 5-ns foot pulse. Using (t_L/τ_R) in Eq. (2) for (t/τ_R), we obtain the gain factors given in Table 39.II for various path lengths.

These simple estimates indicate that the main pulse may be above threshold for significant SRRS if the path length is greater than 25–30 m. Clearly we do not wish to operate the upgrade under these conditions, because of the deterioration in beam quality and beam-to-beam energy balance that would result. Since the SRRS process depends on the detailed laser pulse shape, the estimates given here

Table 39.II Exponential gain factor for stimulated rotational Raman scattering

Propagation distance (m)	10	20	30	40
Gain factor for foot pulse	6	12	19	25
Gain factor for main pulse	19	29	36	42

TC2632

should be treated with caution. More realistic calculations and experimental investigations are clearly needed: If SRRS should be found to present a problem, one possible remedy would be to incorporate beam tubes for a portion of the ~40-m beam path.

The second concern arises from second-order propagation effects associated with the angularly dispersed beams generated using SSD.[8] The angular dispersion causes the projections of the wave vectors of the different frequency components in the propagation direction to have a small nonlinear frequency dependence. As a result, the relative phases of these components change slowly as the pulse propagates, and, after long distances, significant amplitude modulation can develop. The amplitude modulations are greater at higher modulation frequencies and bandwidths. As an example, Fig. 39.7 shows the temporal pulse shape of an initially Gaussian beam of 600-ps FWHM, modulated at 10 GHz with a bandwidth of 3 Å (the baseline SSD parameters for the upgrade), after propagation through 40 m with an angular dispersion of 50 μrad/Å. These parameters are representative of typical operating conditions for the upgrade. Considerable structure is seen in the temporal pulse shape. This modulated pulse shape would not be "seen" by the target, as the times at which intensity maxima occur vary across the beam cross section, and each point on the target sees the intensity integrated over the beam cross section because of the spatial averaging afforded by the DPP's; however, these modulations have the potential for damaging optical components and coatings and are best avoided. Whether or not actual damage will occur as a result of these modulations is by no means certain, since the time-integrated energy loading is unaffected. In addition, a margin of error is built into the baseline design that allows for 1.8:1 modulations in the UV energy loading.

This propagation effect must be considered throughout the system. It is minimized in the IR portion, since the grating plane is image relayed through the system and up to the frequency-conversion crystals. At each image plane of the grating the phase relationships of the various frequency components are restored to their initial values, and the purely phase-modulated character of the pulse is recovered. However, significant intensity modulations can develop at intermediate points between relay planes, and the design of the optical layout must ensure that these modulations do not lead to damage. It is especially important to minimize intensity modulations at the amplifiers and frequency-conversion crystals by locating these components near relay planes,

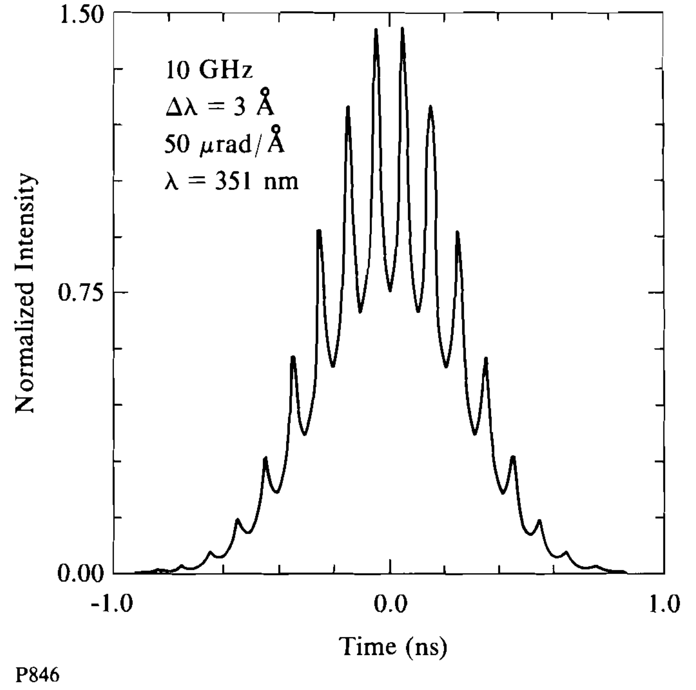

Fig. 39.7
Normalized intensity as a function of time at a point in the cross section of a beam modulated at 10 GHz with a bandwidth of 3 Å, with an angular dispersion of 50 μrad/Å, after propagation through 40 m.

since high intensities increase the risk of self-focusing in laser glass and also lead to reduced frequency-conversion efficiencies. Calculations similar to that of Fig. 39.7 are needed at each stage in the system.

Should the intensity modulations associated with the propagation of UV radiation to the target chamber lead to damage problems, an obvious solution would be to image-relay the UV beam through this path. By doing so, the potential SRRS problem would also be avoided, as a substantial portion of the beam propagation would be through evacuated tubes. While the need for this alternative has not yet been established, it has the merit that possible problems associated with both SRRS and SSD beam propagation would be simultaneously overcome. Detailed calculations and propagation experiments are planned to clarify this issue.

Target Area

The target-mirror structure (see Fig. 39.8) will be highly modular, with five-fold rotational symmetry about the vertical axis reflecting the soccer-ball symmetry in the beam placements. The design provides for segmented platforms and integrates the optical mounts with structurally rigid hexagonal beam tubes. The target mirrors are mounted in boxes on the ends of the beam tubes, which may also serve to provide an isothermal environment for optical components. The beam-transport geometry is such that no angle of incidence at a target mirror will exceed 60°.

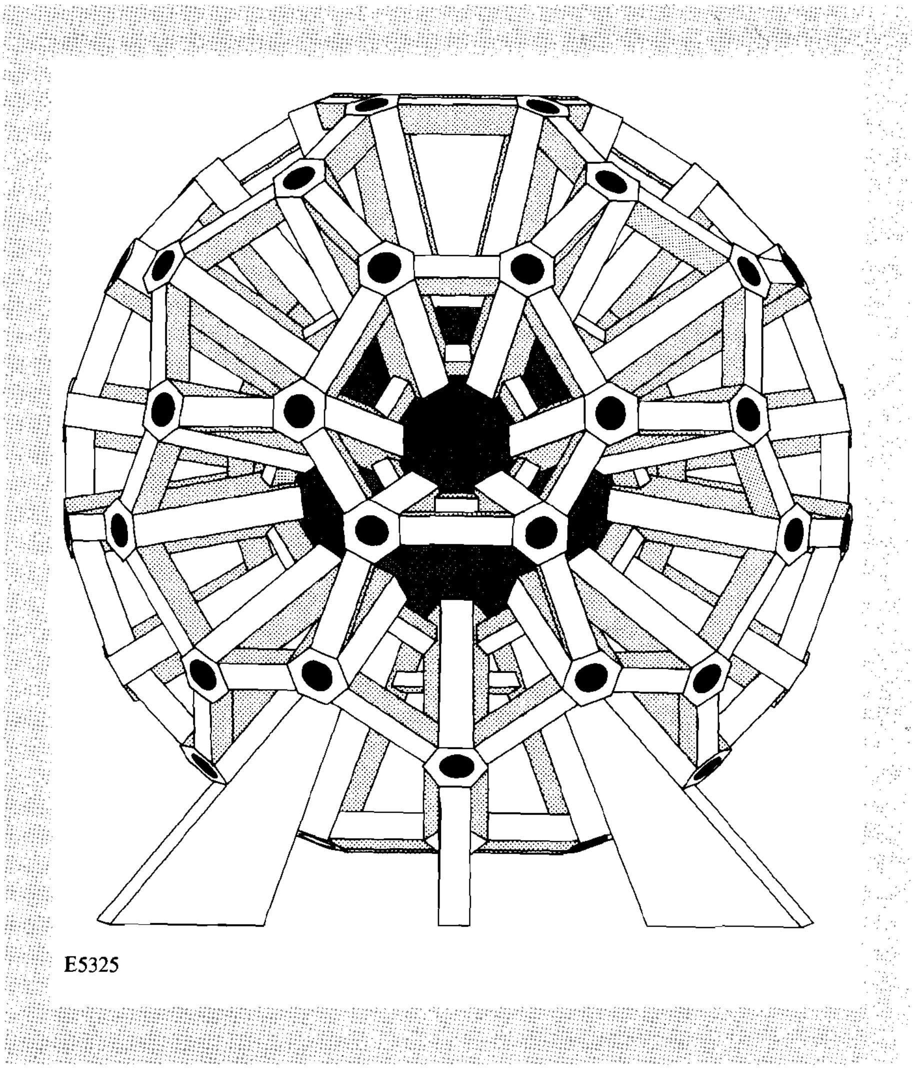

Fig. 39.8
Target-mirror structure for the OMEGA Upgrade.

The target chamber will be 1.8 m in radius and will be constructed out of aluminum alloy, aircraft titanium, or stainless steel. It will also make full use of the soccer-ball geometry. In addition to the 60 beam ports (of diameter 30 cm), there will be 32 diagnostic ports, 20 of large diameter (60 cm) on the hexagonal faces and 12 of smaller diameter (45 cm) on the pentagonal faces. The large diagnostic ports will be particularly useful for instruments requiring a large solid angle, such as a high-resolution neutron time-of-flight spectrometer. Alternatively, they may be fitted with a reducing flange to allow for the use of existing OMEGA instruments. The present complement of OMEGA diagnostics (with modifications where appropriate) will be available for the upgrade. The upgrade target-area design will actually allow a greater free volume for the placement of diagnostic instruments than is presently the case on OMEGA, because beams are transported to the target-mirror structure from the outside, rather than between the target mirrors and the target chamber.

The high neutron yields anticipated for the upgrade have led us to consider what additional shielding of the target area may be necessary. We have undertaken an extensive joint study with Grumman Aerospace to model the potential adverse effects of neutrons on the target chamber, the target bay, and surrounding areas. We have modeled prompt radioactivity in both silicon semiconductor devices and biological tissue, and the build-up of nuclear activation for a typical target-shot schedule. We have included interactions with the experimental target chamber, the turning-mirror structures, optics, electronics, optoelectronics, building walls, and associated structures, and we have investigated a variety of path configurations for neutron transport.

As a result of this study, additional shielding will be required, and some operating procedures will be revised to limit potential radiation exposure to personnel. For example, the area directly underneath the target chamber, which presently houses the experimental control area, will be remotely operated during a DT-filled target shot, and a "cool down" period between a high-yield implosion and personnel re-entry into the target bay may be necessary. Radiation-monitoring detectors connected to computer-controlled interlocks will be installed in order to eliminate the possibility of inadvertent entry of personnel during cool-down periods and to maximize personnel safety. This study is described in more detail in the following article.

Transverse Stimulated Brillouin Scattering

Transverse stimulated Brillouin scattering (TSBS) has been observed in many laser systems.[27-29] It involves the generation of an acoustic wave that propagates in a direction perpendicular to the direction of the incident laser within an optical material. TSBS must be avoided as acoustic intensities can be large enough to fracture an optical element. We have investigated this process and found that it is not a concern for the OMEGA Upgrade.

The equations for TSBS are similar in form to the equations describing SRRS [Eqs. (1) and (2)], with the Raman gain and response time, g_R and τ_R, replaced by the Brillouin gain and response time, g_B and τ_B, and with z replaced by an interaction length within an optic transverse to the laser propagation direction. Generation of TSBS is most likely to occur in the fused-silica substrates near the target chamber. We estimate the gain factor G using parameters reported for fused silica[28,29]: $g_B = 4.48$ cm/GW at 488 nm, and $\tau_B = 1.0$ ns. For z in the main beam we use 21 cm, the length of the largest chord within the annulus $[2(R_2^2 - R_2^1)^{1/2}$ where R_2 and R_1 are the outer and inner radii, approximately equal to 12 cm and 6 cm, respectively, from Fig. 39.2]. For the foot pulse, $z = 9.5$ cm from Fig. 39.2. Again we use intensities 4.63 GW/cm^2 for the 0.5-ns main pulse and 0.83 GW/cm^2 for the 5-ns foot pulse.

Here, the transient formula [Eq. (2)] gives $G = 29.0$ for the main pulse. For the foot pulse, the process is intermediate between the transient and steady-state regimes, which give $G = 21.6$ and 35.3, respectively. (Note that the TSBS response time of 1 ns is much longer than the SRRS response time.) From these figures and the same criterion that G must reach 30–35, it is unlikely that TSBS will prove to be a problem. In addition, the gain for the TSBS process has been shown to decrease significantly with the introduction of just a small amount of bandwidth (a fraction of an angstrom in the IR) onto the laser,[29] substantially less than the bandwidth we plan to use with SSD. TSBS is therefore not a concern for the OMEGA Upgrade.

Alignment

The upgrade alignment system will use two wavelengths, unlike the current system that is aligned from the oscillator to the target in the IR. While this will increase complexity, it will eliminate the two main disadvantages of single-wavelength alignment: the transport mirrors will no longer need dual IR/UV coatings, and it will not be necessary to translate the focus lenses through ~ 109 mm after IR alignment to compensate for their chromatic shift. The IR portion of the laser will be aligned using a 1054-nm YLF laser, together with sensor packages at two locations within each laser chain consisting of a CCD camera, imaging optics, and a shutter to protect the package during a laser shot. The UV portion will be aligned using a 351-nm laser injected through a fiber optic at the UV focus of the IR spatial filter following the last amplifier.

At the heart of the alignment system will be ten mobile full-aperture sensors using all-reflecting achromatic optics, arranged in two stacks of five each, one stack for each side of the laser bay. The sensors will view small fractions of the IR beam energies transmitted through the first mirrors past the frequency-conversion crystals (the "end mirrors"). Each stack will be moved sequentially to six locations to accomplish IR beamline alignment and IR-to-UV alignment. Finally, target alignment will be done by moving the sensors to a seventh location where they will view UV reflections from a surrogate target transmitted back through the end mirrors and reflected by a roving fold mirror, again five beamlines at a time corresponding to six locations of the fold mirror.

Laser Diagnostics and Control Systems

The laser-alignment, diagnostic, and power-conditioning subsystems all rely heavily on computer control and data-acquisition systems. On the current OMEGA laser these systems are largely independent; for the upgrade, developments in network technology will be used to facilitate high-speed communication among the different systems.

Beam-energy measurements are required at various points in the laser chain. The most important measurement is made just after the frequency-conversion crystals, where a Fresnel-reflection pickoff from an uncoated surface is used to transport 4% of the beam energy into a diagnostic package. This is similar to the multiwavelength energy-sensing system (MESS) currently used on OMEGA, except that two integrating spheres will be used, one for the main pulse and one for the foot pulse. The optical layout will ensure that the co-propagated aperture is relayed to the rear surface of the first (main-pulse) integrating sphere, so that the foot pulse will pass through to the second integrating sphere. Separate measurements will therefore be possible for the main and foot pulses at all three wavelengths (1054 nm, 527 nm, and 351 nm).

In order to ascertain the UV energies actually incident on target, accurate measurements of the transport losses from the pickoff to the target are required for each beam line. At present, these losses are measured by a small positionable integrating sphere, which is inserted into the center of the target chamber and successively pointed in each of the 24 beam directions. A similar system will be used for the upgrade.

Summary

We have presented an overall description of the preliminary design for the OMEGA Upgrade. This design is based on existing technology and available optical materials; in addition, it has the potential to benefit from a number of new developments and extensions of existing technology that are anticipated to mature in the near future. We have identified areas where further studies and prototyping are necessary before arriving at the final design. We are aware of no reason why the upgrade should not be able to provide the additional laser energy, uniformity, flexibility, and pulse-shaping capabilities required for future research in direct-drive laser fusion on the OMEGA system.

ACKNOWLEDGMENT

This work was supported by the U.S. Department of Energy Office of Inertial Fusion under agreement No. DE-FC03-85DP40200 and by the Laser Fusion Feasibility Project at the Laboratory for Laser Energetics, which has the following sponsors: Empire State Electric Energy Research Corporation, New York State Energy Research and Development Authority, Ontario Hydro, and the University of Rochester. Such support does not imply endorsement of the content by any of the above parties.

REFERENCES

1. *New Scientist*, 31 March 1988, p. 36.
2. C. Vaughan, *Science News* **135**, 56 (1989).
3. D. Eimerl, *IEEE J. Quantum Electron.* **QE-23**, 1361 (1987).
4. R. S. Craxton, *IEEE J. Quantum Electron.* **QE-17**, 1771 (1981).
5. LLE Review **38**, 79 (1989).
6. Y. Kato *et al.*, *Phys. Rev. Lett.* **53**, 1057 (1984).
7. LLE Review **33**, 1 (1987).
8. S. Skupsky, R. W. Short, T. Kessler, R. S. Craxton, S. Letzring, and J. M. Soures, to be published in *J. Appl. Phys.* See also LLE Review **37**, 29 (1988); LLE Review **37**, 40 (1988).
9. J. T. Hunt, P. A. Renard, and W. W. Simmons, *Appl. Opt.* **16**, 779 (1977).
10. L. M. Frantz and J. S. Nodvik, *J. Appl. Phys.* **34**, 2346 (1963).

11. W. E. Martin and D. Milam, *IEEE J. Quantum Electron.* **QE-18**, 1155 (1982).
12. W. W. Simmons, J. T. Hunt, and W. E. Warren, *IEEE J. Quantum Electron.* **QE-17**, 1727 (1981).
13. W. W. Simmons and W. E. Warren, presented at *SPIE Technical Symposium on Applications of Artificial Intelligence*, Orlando, Florida, 31 March 1986. Available as Lawrence Livermore National Laboratory Report UCRL 94380.
14. We are indebted to J. Lawson of LLNL for the availability of this code.
15. P. LeFur and D. H. Auston, *Appl. Phys. Lett.* **28**, 21 (1976).
16. G. Mourou and W. Knox, *Appl. Phys. Lett.* **35**, 492 (1979).
17. S. D. Jacobs, K. A. Cerqua, K. L. Marshall, A. Schmid, M. J. Guardalben, and K. J. Skerrett, *J. Opt. Soc. Am. B* **5**, 1962 (1988).
18. J. C. Lee, S. D. Jacobs, T. J. Kessler, and N. Van Lieu, *Technical Digest-CLEO '89*, Baltimore, MD, 1989.
19. M. J. Lubin, J. M. Soures, and L. M. Goldman, *J. Appl. Phys.* **44**, 347 (1973).
20. Laser Program Annual Report—1977, Lawrence Livermore Laboratory, Livermore CA, UCRL 50021-77 (1978), pp. 2-142 to 2-145.
21. J. Hunt *et al.*, UCID-19086, p. 10 (1981).
22. LLE Review **37**, 16 (1988).
23. D. Smith and A. Schmid, unpublished data.
24. M. A. Henesian, C. D. Swift, and J. R. Murray, *Opt. Lett.* **10**, 565 (1985).
25. W. Kaiser and M. Maier, in *Laser Handbook*, Vol. 2, edited by F. T. Arecchi and E. O. Shulz-Dubois, (N. Holland Publ. Co., Amsterdam, 1972), p. 1077.
26. V. S. Averbakh, A. I. Makarov, and V. I. Talanov, *Sov. J. Quantum Electron.* **8**, 472 (1978).
27. J. L. Emmett and L. Schalow, *Phys. Rev. Lett.* **170**, 358 (1968).
28. J. M. Eggleston and M. J. Kushner, *Opt. Lett.* **12**, 410 (1987).
29. J. R. Murray *et al.*, Laser Program Annual Report—1989, Lawrence Livermore National Laboratory, Livermore, CA, UCRL 99914.